

On the response of semitransparent nanoparticulated films of LuPO₄:Eu in poly-energetic X-ray imaging applications

I. E. Seferis¹ · J. Zeler¹ · C. Michail² · I. Valais² · G. Fountos² · N. Kalyvas² · A. Bakas³ · I. Kandarakis² · E. Zych¹

Received: 30 September 2015 / Accepted: 18 April 2016 / Published online: 26 April 2016
© The Author(s) 2016. This article is published with open access at Springerlink.com

Abstract In the present work, we demonstrate the fabrication technique of highly translucent layers of nanoparticulated (~ 50 nm) LuPO₄:Eu phosphor, present their basic luminescent properties and give results of their performance in a planar imaging system coupled to a CMOS photodetector. For comparison, the imaging performance of an opaque Gd₂O₂S:Eu phosphor screen prepared by sedimentation is also shown. The X-ray detection parameters as well as the luminescence efficiency of the investigated films were discussed. Results show that the in-line transmittance at ~ 600 – 700 nm, in the range of the phosphor luminescence, varies with respect to the thickness of the films from 40 to 50 % for a film of 67 μm thick to 4–12 % when the thickness increases to 460 μm . Yet, X-ray detection parameters get enhanced as the thickness of the films increases. Those results affect the luminescence efficiency curves of the films under poly-energetic X-ray radiation of various tube energies. The normalized noise power spectrum values were found similar for LuPO₄:Eu films and a phosphor screen made using commercial Gd₂O₂S:Eu powder. The detective quantum efficiency of our films is clearly lower compared to the Gd₂O₂S:Eu screen from 2 to

10 cycles mm^{-1} frequency range while the modulation transfer function is lower from 0 to 5.5 cycles mm^{-1} frequency range. The acquired data allow to predict that high-temperature sintering of our films under pressure may help to improve their imaging quality, since such a processing should increase the luminescence efficiency without significant growth of the grains and thus without sacrificing their translucent character.

1 Introduction

Improvement in detection of ionizing particles requires a constant development of scintillator materials—their performance and optical quality. Not only a high density and high Z-number to efficiently absorb X- and γ -rays are of great importance, but also high scintillation efficiency, low level of afterglow, uniformity in the emitting center (activator) distribution within the scintillator body to ensure good energy resolution and generally uniform properties within the whole scintillator body.

Scintillator materials are used in various applications such as medical imaging, high-energy physics, airport security and industrial control [1]. In contrast to detection of γ -particles, recording X-rays does not require transparent scintillators. Even layers of powder phosphors may be appropriate. Yet, the scattering of scintillation light within the scintillator/X-ray phosphor layer plays a very important role and affects resolution and contrast of images greatly. In imaging applications, transparent scintillator/X-ray phosphor materials appear to limit images resolution due to high scintillating light diffusion. To reduce this effect, pixelated detectors were produced and tested [2, 3]. While the improvement was significant, the technology appeared quite expensive as laser etching was necessary.

✉ E. Zych
eugeniusz.zych@chem.uni.wroc.pl

¹ Faculty of Chemistry, University of Wroclaw, 14. F. Joliot-Curie Street, 50-383 Wroclaw, Poland

² Radiation Physics, Materials Technology and Biomedical Imaging Laboratory, Department of Biomedical Engineering, Technological Educational Institute of Athens, Egaleo, 122 10 Athens, Greece

³ Department of Medical Radiological Technology, Technological Educational Institute of Athens, 122 10 Athens, Greece

Consequently, layers of powder phosphors are still in use, and thus, any improvement in their properties is important.

Although the light scattering is beneficial for images quality, when excessive, it leads to significant signal output reduction which is obviously deleterious for an image quality. Scattering of light occurs in optically inhomogeneous materials due to the different refractive index and in non-isotropic crystals by birefringence [4]. It has been shown theoretically [5, 6] and demonstrated in practice [7] that diminishing scattering losses in polycrystalline layers is possible in phosphor bodies of reduced grain sizes well below the (emitted) radiation wavelength. This problem was in depth theoretically treated [8] and it was showed that for phosphors emitting in red the optimal imaging resolution properties are achieved when the phosphor particles are about 200 nm in diameter. Nevertheless, the luminescence efficiency of the scintillating screen at this case gets reduced. So a compromise between acceptable resolution properties and signal level properties seems to be the key for an overall acceptable image quality.

Activated with rare earth lutetium-based scintillator materials were demonstrated to have an extraordinary stopping power due to their high-densities and high-effective *Z*-numbers. In many cases, their scintillation efficiency is also high and in some cases truly extraordinary [9–11]. Also LuPO₄-based phosphors were reported as efficient scintillators [12]. Since technology of making high-quality large single LuPO₄ crystals was never developed, their polycrystalline screens appear the only perspective for their application in imaging.

In the present work, we demonstrate the fabrication technique of semitransparent layers of nanoparticulated (~50 nm) LuPO₄:Eu, present their basic luminescent properties and give results of their performance in a planar imaging system with CMOS photodetector. Layers of LuPO₄:Eu with different Eu content and different grain sizes have been researched, and the results are discussed.

Achieved modulation transfer function (MTF), the noise power spectrum (NPS) and the detective quantum efficiency (DQE) under poly-energetic X-ray radiation will be presented and discussed. Compared to a Gd₂O₂S:Eu, opaque phosphor screen of 91 μm thickness will be given. Efficiency under X-rays excitation was also investigated in terms of absolute efficiency, for various X-rays energies.

2 Materials and methods

2.1 Synthesis and film preparation

Two kinds of LuPO₄:*x* %Eu (*x* = 5 and 15) compact layers were prepared using hydrothermally synthesized precursors. The standard procedure was as follow: Lu₂O₃ (Stanford Materials Corporation, 99.995 %) and Eu₂O₃ (Stanford Materials Corporation, 99.999 %) were dissolved in diluted HNO₃ (Eurochem, cz.d.a) at 90 °C. Appropriate amount of (NH₄)₂HPO₄ was added to the solution (see Table 1 for details). The acidity of the mixture was adjusted to pH 2 using NH₃ solution. The final suspension was transferred into stainless steel autoclave, with Teflon lining, and heated at 230 °C for 10 h. After cooling to room temperature (RT), the powders were separated, washed several times with water–ethanol mixture and dried at 80 °C for 12 h. For the preparation of the semitransparent films, the powders mixed with some water were transferred into plastic beakers. The suspensions were left at room temperature until the water evaporated. Four films of different thicknesses (65, 100, 220 and 460 μm) were obtained with 15 % Eu concentration, and one with 5 % Eu (375 μm). Such layers were then heated at 1000 °C for 2 h in air. Figure 1 presents the samples' photograph and proves their translucency. For comparison, an opaque screen was prepared by sedimentation of a powder of 1–3 μm grains of LuPO₄:5 %Eu. Procedure of making this

Table 1 Exemplary amounts of starting reagents for the synthesized powders

Starting composition (g)				Processing temperature (°C)/time (h)	Eu Conc. (mol%)
Lu ₂ O ₃	Eu ₂ O ₃	(NH ₄) ₂ HPO ₄	pH		
2.1097	0.0982	1.4739	0	230/10	5
2.1097	0.0982	1.4739	2		5
1.9038	0.2971	1.4866	2		15

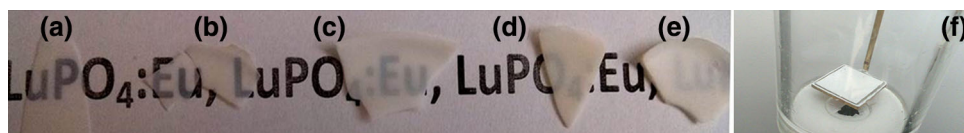


Fig. 1 LuPO₄:Eu films heated at 1000 °C in air with different thicknesses: **a** 65 μm, **b** 100 μm, **c** 220 μm, **d** 375 μm, **e** 460 μm. Also opaque LuPO₄:5 %Eu screen is shown inside the sedimentation tube (1F) after removal of the solution (see Fig. 2c for the powder morphology)

screen, whose thickness reached 200 μm , was presented previously [13]. The powder for this screen was prepared from the raw powder of hydrothermally synthesized (see above) LuPO₄:Eu in pH 0, which was additionally heated at 1000 $^{\circ}\text{C}$ for 5 h in air.

2.2 Structure, morphology and spectroscopic measurements

The powder X-ray diffraction patterns were measured using a D8 Advance diffractometer (Bruker) with Ni-filtered CuK _{α 1} radiation ($\lambda = 1.540596 \text{ \AA}$) in the range of $2\theta = 15^{\circ}$ – 65° , with the step of $2\theta = 0.008^{\circ}$. The morphology of the ceramics was examined using SEM/FIB—FEI Helios NanoLab 450 HF (FEI Company) scanning electron microscope.

The room-temperature photoluminescence emission (PL) and excitation (PLE) spectra, as well as the luminescence decay traces (DEC), were recorded with a FLS980-sm Fluorescence Spectrometer from Edinburgh Instruments Ltd., using a 450 W continuous Xe arc lamp (PL and PLE) and 60 W Xenon flash lamp (DEC), as an excitation sources. TMS302-X single grating excitation and emission monochromators of 30 cm focal lengths were used. The luminescence light was recorded by a Hamamatsu R928P high-gain photomultiplier detector. The emitted spectra were corrected for the recording system efficiency, and the excitation spectra were also corrected for the incident light intensity. The room-temperature X-ray-excited luminescence (RL) spectra were recorded upon white X-rays taken from a Cu X-ray tube, using 40 kV and the 10 mA current. The emitted photons were collected with a 74-UV lens connected to a QP600-2-SR-BX waveguide which transferred the luminescent light to an Ocean Optics HR2000CG-UV-NIR Spectrometer. A SpectraSuite dedicated software was used to record the spectra.

2.3 X-ray experimental setup

Experiments were performed using a Philips Optimus X-ray unit. The radioluminescence efficiency measurements were taken for X-ray tube voltage varying in the range of 50–120 kVp and tube current product 63 mAs. The experimental setup comprised a light integration sphere (oriel 70451), coupled to a photomultiplier (EMI 9798 B) with an extended sensitivity S-20 photocathode. The photomultiplier current was amplified and fed to a Cary 401 electrometer.

For the imaging quality measurements, an optical readout device including a CMOS Remote RadEye HR

photodiode pixel array was used. The CMOS consists of 1200×1600 pixels with 22.5 μm pixel pitch and a fill factor of 0.8. The films were held using a thin polyurethane foam layer for compression between the films and a 1-mm-thick graphite cover. The films were directly coupled to the photodiode array, while at the top side neither absorptive nor reflecting layer was used. The experiments were carried out at 70 kVp X-ray energy and 63 mAs tube current product. The source-to-detector distance (SDD) was 180 cm. The exposure rate at the entrance surface of the experimental devices was measured by replacing it with a calibrated dosimeter (Piranha RTI Electronics), while the photon fluence was measured with a portable Amptek XR-100T spectrometer.

2.4 X-ray detection parameters

The radiation detection of the films was calculated by the following parameters:

- (a) The quantum detection efficiency (QDE) which provides the ratio of the X-ray quanta absorbed by the films, per incident X-ray quantum, and calculated by Eq. 1 [14]:

$$\text{QDE} = \frac{\int_0^{E_0} \Phi_X(E) (1 - e^{-(\mu_{\text{tot}}(E)/\rho)W}) dE}{\int_0^{E_0} \Phi_X(E) dE} \quad (1)$$

- (b) Energy absorption efficiency (EAE) which gives the ratio of the absorbed X-ray energy per incident X-ray energy and calculated by Eq. 2 [14]

$$\text{EAE} = \frac{\int_0^{E_0} \Psi_X(E) (\mu_{\text{tot,en}}(E)/\mu_{\text{tot}}(E)) (1 - e^{-(\mu_{\text{tot}}(E)/\rho)W}) dE}{\int_0^{E_0} \Psi_X(E) dE}, \quad (2)$$

where Φ_X and Ψ_X are the incident X-ray photon fluence and incident X-ray energy fluence, respectively, measured with the Amptek spectrometer. $\mu_{\text{tot,en}}(E)$ is the total energy absorption coefficient of the scintillator, which includes all mechanisms of energy deposition locally at the point of X-ray interaction within the scintillators mass. All secondary photons, created just after the primary interaction effect, were assumed to escape the irradiated material [15]. $\mu_{\text{tot}}(E)$ is the X-ray total attenuation coefficient. The values of the coefficients were taken from tabulated data [16].

2.5 X-ray efficiency measurements

The absolute efficiency was determined by measuring the light energy flux emitted by the irradiated screen and dividing by the incident exposure rate, according to Eq. 3 [17].

$$AE = \Psi_A/X, \quad (3)$$

where AE was expressed in units of $\mu\text{W m}^{-2}/\text{mR s}^{-1}$, where $\mu\text{W m}^{-2}$ corresponds to the light energy flux (Ψ_A) and mR s^{-1} to the exposure rate (X). For simplicity, the notation efficiency unit (EU) was used ($1\text{EU} = \mu\text{W m}^{-2}/\text{mR s}^{-1}$).

2.6 Imaging quality measurements

2.6.1 Modulation transfer function (MTF)

The modulation transfer function (MTF) was used to characterize the resolution properties of an X-ray imaging system, describing the variation of contrast with spatial frequency [18–20]. The MTF was measured by means of a PTW Freiburg tungsten edge test device. Images of the edge, placed at a slight angle, were obtained. The edge spread function (ESF) was calculated by the extraction of a $1 \times 1 \text{ cm}^2$ ROI, which covers a large portion of the active area of the CMOS sensor ($2.7 \times 3.6 \text{ cm}$), with the edge roughly at the center. The ESF was differentiated to obtain the line spread function (LSF). Finally, the normalized LSF was Fourier transformed to give the pre-sampling MTF.

2.6.2 Normalized noise power spectra (NNPS)

Noise power spectrum (NPS) is an image quality metric that provides a quantitative description of the amount and frequency of the noise contained within a particular imaging system. The area of analysis was 1024×1024 pixels. Half overlapping ROIs with a size of 128×128 pixels were then taken from the sub-images. A total of 128 ROIs were taken from each flood image. For all the ROIs

taken from each image, 2D fast Fourier transform (FFT) of each ROI was calculated and added to the NPS ensemble. NNPS was obtained by dividing NPS by the square of the corresponding mean pixel value, and afterward, the ensemble average was obtained [21, 22].

2.6.3 Detective quantum efficiency (DQE)

The detective quantum efficiency describes the output signal-to-noise ratio, associated with the image produced by the detector, and is a measure of the combined effects of the signal and noise performance of an imaging system, expressed as a function of spatial frequency. The DQE of the system was evaluated by Eq. 4 [23]:

$$DQE = \frac{MTF^2(f)}{K_x q NNPS(f)}, \quad (4)$$

where q is the number of photons per air kerma unit (μGy) per mm^2 , determined by dividing the number of photons per mm^2 (measured with the portable X-ray spectrometer) with the corresponding air kerma value (measured with the Piranha dosimeter). K_x is the air kerma value at the surface of the detector in μGy .

3 Results and discussion

Figure 2 shows SEM images of the nanoparticulated films surface before and after heat treatment at $1000 \text{ }^\circ\text{C}$ in air. The raw and heat-treated films have similar morphology; thus, the thermal processing did not lead to any noticeable mass transfer between the grains, and thus, they did not grow (Fig. 2a, b). The average grains size is about 50 nm and its distribution is very narrow. Also grains agglomeration is negligible, and the grains shape is practically spherical. Figure 2c shows the image of the $\text{LuPO}_4:5 \text{ \%Eu}$ powder made at pH 0 (see Table 1) used for the preparation of the opaque screen by sedimentation. The grain size ranges between 1 and $3 \text{ }\mu\text{m}$, and there is no agglomeration observed. The grains of this powder are disk shaped.

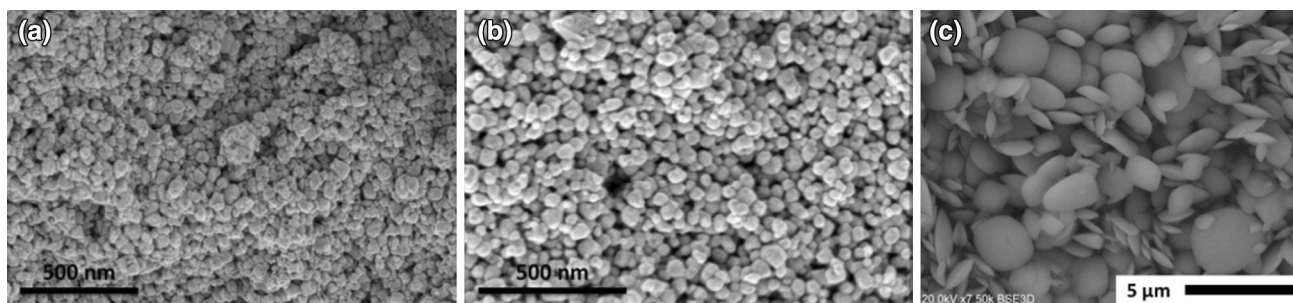


Fig. 2 SEM images of the raw (a) and heated at $1000 \text{ }^\circ\text{C}$ in air (b) $\text{LuPO}_4:\text{Eu}$ films. c SEM image of the $\text{LuPO}_4:5 \text{ \%Eu}$ powder used for the opaque screen preparation (see Fig. 1f)

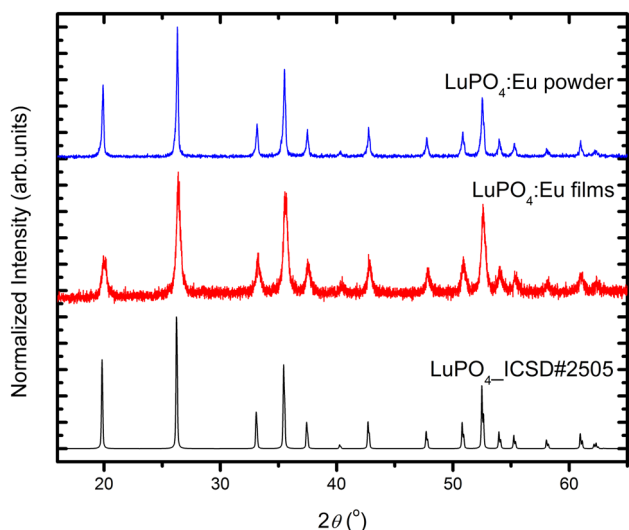


Fig. 3 XRD patterns of LuPO₄:Eu films heated at 1000 °C and the LuPO₄:5 %Eu powder used for the screen preparation, compared with a simulated pattern of a tetragonal LuPO₄

Figure 3 shows the XRD patterns of LuPO₄:Eu films and the pattern of the LuPO₄:5 %Eu powder used for the preparation of the screen. For comparison, a simulated pattern of tetragonal LuPO₄ (ICSD #2505) is also given. It is obvious that all the phosphates are composed of phase-pure LuPO₄:Eu phosphors. The LuPO₄:5 %Eu powder gives much narrower lines, in agreement with the much larger size of the grains (see Fig. 2).

Figure 4a shows typical room-temperature (RT) photo- and radio-luminescence spectra of LuPO₄:15 %Eu films after heat treatment at 1000 °C in air together with PLE of the 619.6 nm emission. The PLE spectrum contains well-resolved lines related to ⁷F₀ → ⁵H₃ (~323 nm), ⁵D₄ (~363 nm), ⁵L_J (~380–400 nm), ⁵D₃ (~413 nm), ⁵D₂ (~466 nm) and ⁵D₁ (~537 nm) absorption transitions of Eu³⁺ in LuPO₄. Apart of the sharp lines a trace of the O²⁻ → Eu³⁺ charge transfer broad band below 280 nm can also be seen. Its low efficiency is presumably connected with the fact that it is mostly situated at energies higher than accessible by the instrument used in this research. Presumably, it is located below ~250 nm, where the incident light practically almost totally diminishes. The high energy of the CT transition is justified by quite large interatomic distances in LuPO₄ host. The RL spectrum (blue line) and photoluminescence emission taken upon 394.8 nm excitation (black line) are very similar and contain typical for Eu³⁺ sharp lines connected with the ⁵D₀ → ⁷F_J (J = 1, 2, 3, 4) transitions. Typical decay traces of 593.4 and 619.6 nm under 394.8 nm excitation of LuPO₄:x%Eu are shown in Fig. 4b. They are monoexponential and practically identical for all investigated compositions, independently on the microstructure and Eu content. The derived decay times are 3.0–3.3 ms. Such values of decay time limits the possible applications of the phosphor to stationary X-ray imaging applications. The long decay times and their single exponential character substantiate that there is not present any significant

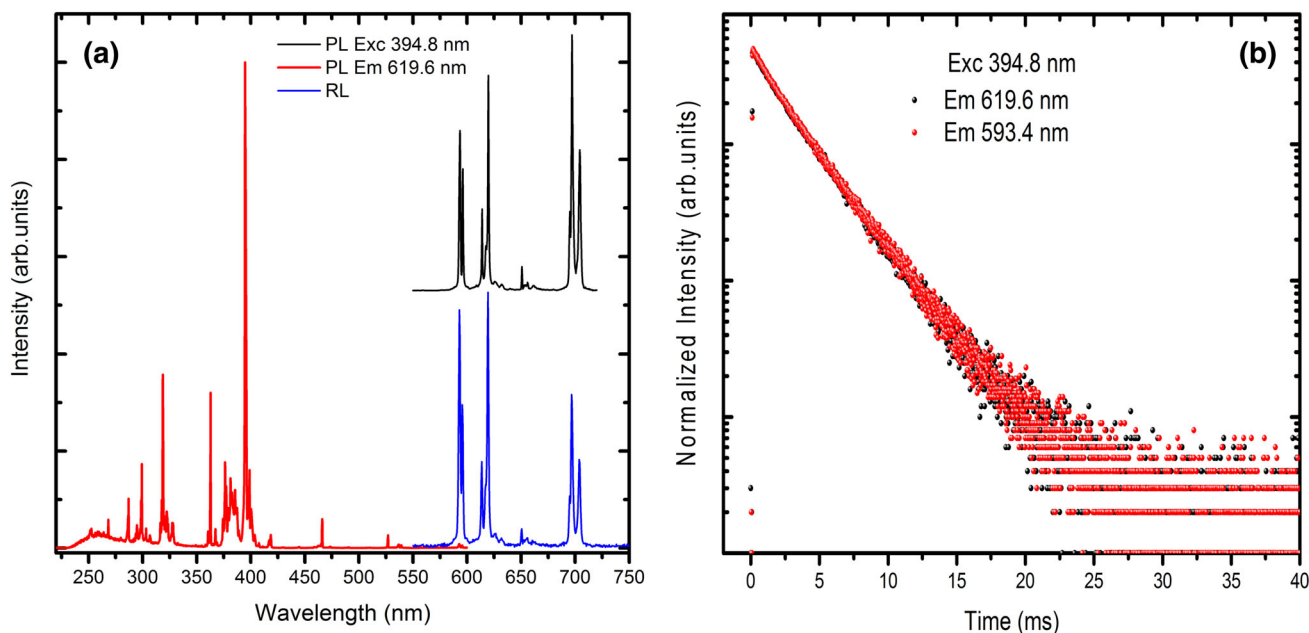


Fig. 4 **a** Excitation spectrum of 619.6 nm emission and emission spectra under X-ray (blue line) and 394.8 nm (black line) excitation, **b** the decay traces of 619.6 and 593.4 nm emissions under 394.8 nm excitation of LuPO₄:15 %Eu film

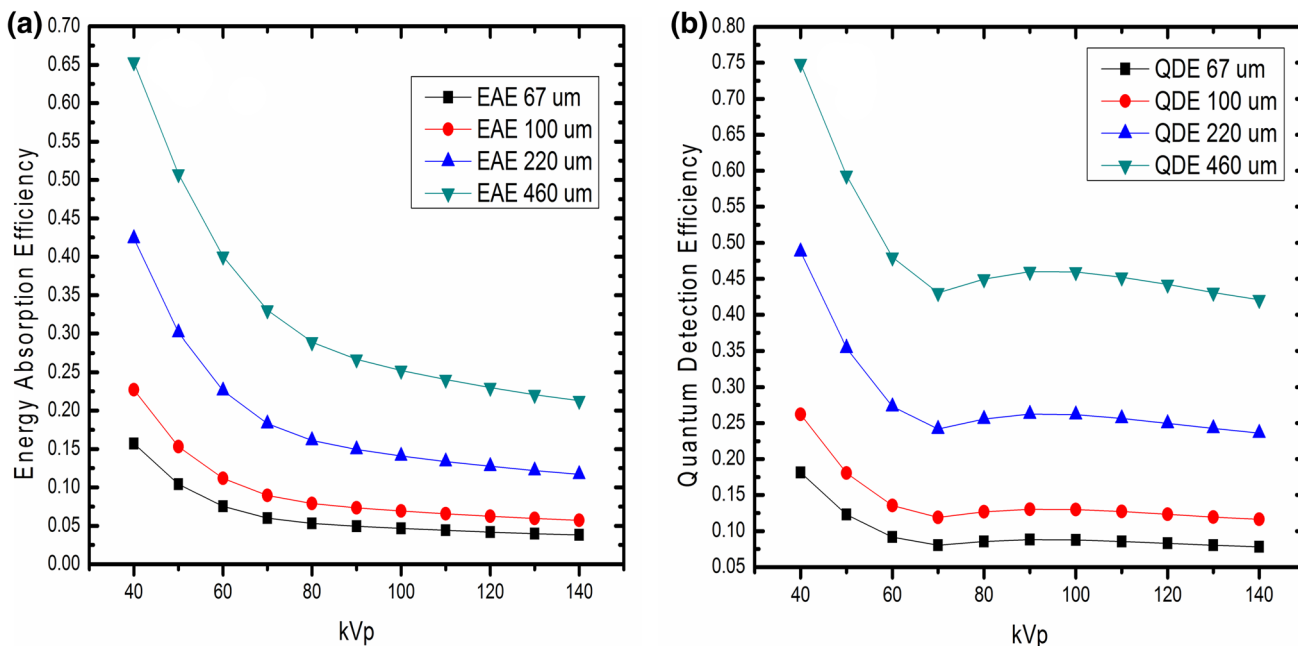


Fig. 5 Calculated EAE (a) and QDE (b) curves of the LuPO₄ films

quenching of the Eu photoluminescence in the investigated materials.

Figure 5 shows the calculated QDE and EAE of all LuPO₄:Eu films depending on X-rays energy (kVp). Both EAE and QDE values get reduced as the thickness of the films decreases, mostly because the high-energy X-ray photons cannot be efficiently absorbed in thin phosphor layers. Within the whole energy range, we observe that QDE values are higher than EAE ones. This behavior is attributed to the different nature of the total energy absorption coefficient ($\mu_{\text{tot,en}}(E)$) and the total attenuation coefficient ($\mu_{\text{tot}}(E)$). The former includes all the energy absorption mechanisms of primary radiation interaction, neglecting the path that the photons follow after elastic or inelastic scattering. The second is related to the incoherent processes as the photoelectric effect, Compton Effect and pair production, as well as with coherent processes such as Rayleigh scattering. Within this range of energies, the Compton effect is dominating; thus, the energy deposited to the phosphor by the primary radiation is lower than the total absorbed energy. The differences of EAE and QDE for the 70–140 kVp energy range are especially high as at higher energies the Compton scattering becomes progressively more effective. This behavior is also due to the production and emission of K-fluorescence X-rays. After the K-level absorption (63 keV), X-rays are produced and they get either absorbed within the films or they escape. The scintillation photons produced by the K-fluorescence X-rays have both desirable and undesirable aspects. The advantage they bring is the sensitivity increment, while the

drawback is the image degradation, since such X-ray photons increase the noise and lead to artifacts [24].

As we stated in introduction, some transparency is an important advantage of the films as it enhances directly the effectiveness of the scintillation light transmission to the electronic detector. Figure 6 presents the in-line transmittances of all nanoparticulated LuPO₄:15 %Eu phosphor films and of the LuPO₄:5 %Eu film in the visible part of spectrum (see also Fig. 1). Obviously, as the film thickness increases, the in-line transmittance decreases. For the 67 μm film, it reaches about 40–50 % within the red region

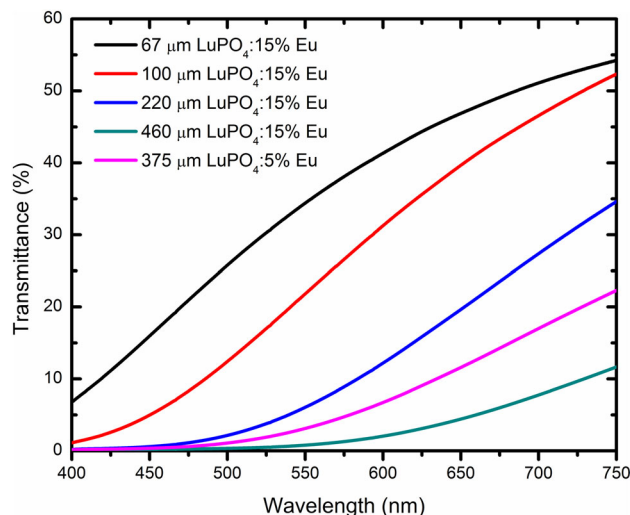


Fig. 6 Transmittance of LuPO₄:Eu films

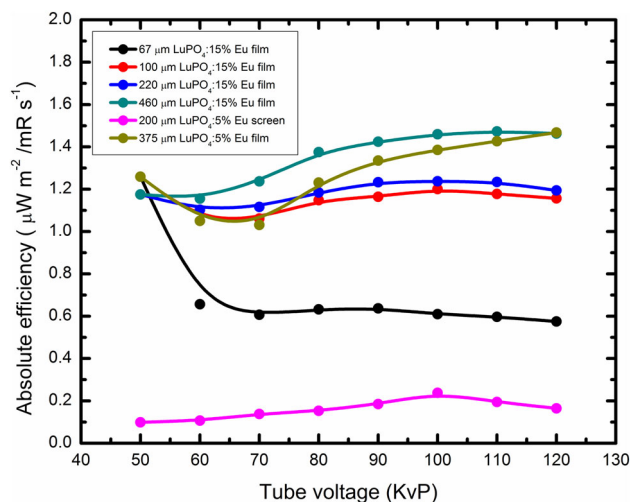


Fig. 7 Absolute efficiency of LuPO₄:Eu films. The absolute efficiency of the LuPO₄:5 %Eu screen is also shown

of the visible light, while for the thickest film (460 μm) the value is only about 4–12 %. Those values provide a quantitative insight of the red emitted photons scattering depending on film thickness and are in good accord with what is seen by eye (Fig. 1).

Figure 7 shows the variation of AE of all nanoparticulated LuPO₄:15 %Eu films with X-ray tube voltage in the range from 50 to 120 kVp. All curves show a decrease in AE from 50 to 60 kVp to become constant for the thinnest film and even increase noticeably for the thicker ones. The decrease between 50 and 60 kVp can be explained by decreasing absorption efficiency with increasing energy of X-rays. The AE drop is the most profound for the 67 μm film, which may be attributed to an especially low attenuation of the photons emitted at the surface of the screen by the low energy incident X-rays (50 kVp). At low energies (50 kVp), the absolute efficiency has higher values for the thin screens (67 and 100 μm), which comes in contrast to the X-ray detection results. Although the EAE and QDE are lower at thin screens than those of thick screens, the high values of the transmittance overbalance the low values of X-ray detection efficiency. The relatively significant increase in AE for tube voltage of 70–80 kVp that was observed for all but the thinnest film should be attributed to the K-absorption edge of Lu around 63 keV of X-rays energy. Above 80–90 kVp, the AE is pretty stable for all films. This confirms that the films thickness is too low to absorb the highest-energy X-rays efficiently. The absolute efficiency values of LuPO₄:5 %Eu film for tube voltage higher than the K-absorption edge follow more increasing trend than the LuPO₄:15 %Eu films. In Fig. 7, the absolute efficiency of the opaque LuPO₄:Eu powder screens of 200 μm thickness and grain size about 500 nm is also shown. The absolute efficiency values are clearly lower

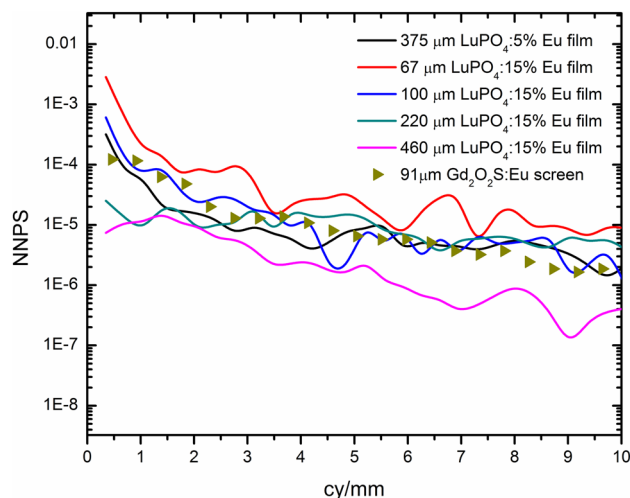


Fig. 8 NNPS of LuPO₄:Eu films. The NNPS of a Gd₂O₃S:Eu screen of 91 μm thickness is also showed

than those of LuPO₄:15 %Eu and LuPO₄:5 %Eu films. Those differences are mainly attributed to the different shape of the grains. The spherical grains emit light uniformly in all directions, while in the case of disk-shaped grains the strong intensity comes out from the edge of the grains. The anisotropic light emission in conjunction with the bigger grain size leads to low light emission of the phosphor screen in transmission mode. The scattering of visible photons, thus their attenuation, is influenced by the scattering coefficient which in turns gets affected by the grain size.

Figure 8 shows the normalized noise power spectra (NNPS), obtained from uniformly exposed images under the same exposure level for all nanoparticulated films. The NNPS presents significantly higher values near the zero frequency for the 67, 100 and 375 μm films, pointing on their higher non uniformities compared to the 200 and 460 μm films. In medium frequencies, this noise is less evident since the Poisson distributed stochastic contributions (X-rays quantum noise, visible photons quantum noise) is prevailed. For higher frequencies, the electronic noise may be of some importance. Comparing the NNPS curves of all films is obvious that the noise levels decreased as the thickness increased. The noise reduction seems to follow the luminescence results. Considering that the number of photons produced per incident X-ray is higher, as the thickness increases, the NNPS values decrease due to better spatial distribution of visible photon on the active area of the detector. Another effect that may contribute to the NNPS values is the film thickness. The greater thickness results in larger light spread giving higher solid angle of the emitting photon beam. This in turn blurs the final image and thus degrades small statistical signal differences (i.e., noise). This behavior is typical of detectors based on

indirect conversion and is determined by the spatial correlation between adjacent pixels that read the same signal because of the light diffusion. Since the luminescence of the opaque screen of $\text{LuPO}_4:5\% \text{Eu}$ was not adequate to give images suitable for image quality evaluation, in this figure the NNPS of a commercial $\text{Gd}_2\text{O}_2\text{S}:\text{Eu}$ powder phosphor opaque screen, of $91\ \mu\text{m}$ thickness, evaluated in previous study [9], is also shown. The noise of this screen at low to medium frequencies seems to follow a similar pattern with the noise levels of the $100\ \mu\text{m}$ film, while at higher frequencies the noise of the granular phosphor screen has decreasing trend. Those differences are due to different grains size of the two screens, leading to different scattering, and thus light diffusion, properties.

Figure 9 shows the MTF curves of all nanoparticulated film screens under the same exposure conditions. As the thickness of the film screens increases, the MTF decreases. It is reasonable that at thicker screens the average distances travelled by the emitted light quanta within the phosphor layers are longer resulting in more extensive light spread, and consequently leading to the degradation in image sharpness and spatial resolution. For the two thickest films (460 and $220\ \mu\text{m}$), the MTF curves practically do not differ, while MTFs for the thinner layers of 100 and $67\ \mu\text{m}$ are higher as the layer's thickness decreases. This is because in thicker films the optical effects, i.e., light scattering, light angular distribution become obviously more potent. This provides a limitation of light diffusion to lower solid angles within the phosphor [25]. In Fig. 9, the MTF of an opaque $\text{Gd}_2\text{O}_2\text{S}:\text{Eu}$ phosphor screen with grain size about $8\ \mu\text{m}$ and thickness of $91\ \mu\text{m}$ is also shown [9]. The MTF values of this screen are higher than the values of the $67\ \mu\text{m}$ screen film in the low to medium frequency

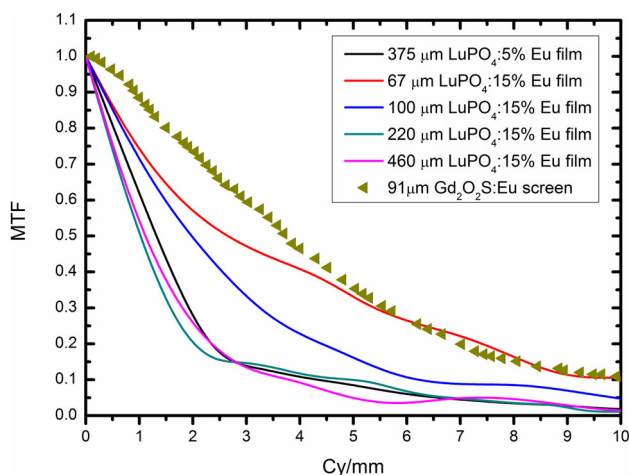


Fig. 9 MTF of $\text{LuPO}_4:\text{Eu}$ films. The MTF of a $\text{Gd}_2\text{O}_2\text{S}:\text{Eu}$ screen of $91\ \mu\text{m}$ thickness is also showed

range, though the thickness is slightly higher. As mentioned above, the grain size of this screen gives rise to much higher scattering of the emitted radiation compared to the film made up of $\sim 50\ \text{nm}$ grains. Thus, the lateral emitted photons become attenuated by scattering before they reach the screen edge and finally the detector. In the high frequency range, the two screens have comparable MTF values.

Figure 10 shows DQE curves for all nanoparticulated film thicknesses, obtained according to (4). The DQE curves of the 67 and $100\ \mu\text{m}$ films show an increase in the spatial frequency range from 0 to $1.2\ \text{cycles}\ \text{mm}^{-1}$. This is due to the fact that NNPS falls off rapidly in this spatial frequency range. Thereafter the reduction rate of the NNPS falls off in contrast to the corresponding MTF curves, contributing to a further decrease in the DQE. The higher DQE values observed for the 220 and $460\ \mu\text{m}$ films up to medium frequencies, while at high frequencies the DQE values are comparable. Although the MTF values of these films are much lower than the thinner screens, the capability of the higher X-ray absorption, in conjunction with the low noise properties, leads to higher DQE values. For comparison purposes, the DQE curve of the opaque $\text{Gd}_2\text{O}_2\text{S}:\text{Eu}$ phosphor screen with grain size about $8\ \mu\text{m}$ and thickness of $91\ \mu\text{m}$ is also shown. In the low spatial frequency range (up to $1.2\ \text{cycles}\ \text{mm}^{-1}$), the DQE values are comparable with the values of the 220 and $460\ \mu\text{m}$ films, while in the medium and high frequency range the $87\ \mu\text{m}$ screen retains high values in contrast to the films. This is due to the higher MTF values of this screen which contributes to higher DQE values.

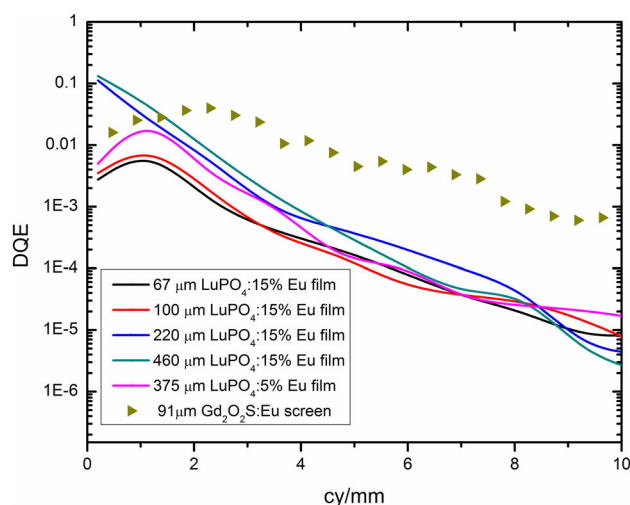


Fig. 10 DQE of $\text{LuPO}_4:\text{Eu}$ films. The DQE of a $\text{Gd}_2\text{O}_2\text{S}:\text{Eu}$ screen of $91\ \mu\text{m}$ thickness is also showed

4 Summary and conclusion

In the present work, the fabrication technique of semi-transparent layers of nanoparticulated (~ 50 nm) LuPO₄:Eu phosphor of two different Eu concentration (5 and 15 %) was presented. The films' basic luminescent properties were reported and results of their performance in a planar imaging system with CMOS photodetector were systematically investigated and all the important X-ray detection parameters as well as the luminescence efficiency of the investigated films were measured and discussed. The results were related to performance of an opaque LuPO₄:5 %Eu screen of 200 μm thickness and grain size ranged to 1–3 μm.

The excitation and emission spectra as well as the decay curves are identical for all examined compositions, independently on the microstructure and Eu concentration, indicating that concentration quenching as well as size effects detrimental for the luminescence is not observed. The monoexponential decay traces give decay times of $\tau \sim 3.0\text{--}3.3$ ms, which proves good optical quality of the films and is acceptable for stationary X-ray applications.

Results show that the in-line transmittance at ~ 600–700 nm varies with respect to the thickness of the films from 40 to 50 % for a film of 67 μm thick to 4–12 % when the thickness increased to 460 μm. X-ray detection parameters get improved as the thickness of the films increases. Those characteristics affect the luminescence efficiency curves of the films under poly-energetic X-ray radiation of various tube energies. The opaque screen of LuPO₄:5 %Eu gives very low values of luminescence efficiency, since the emitted photons experience higher scattering due to the size and the shape of the grains.

Since the luminescence of the opaque screen of LuPO₄:5 %Eu was not adequate to give images suitable for image quality evaluation, the results of the nanoparticulated LuPO₄:Eu films were compared with the results of a previously studied commercial Gd₂O₂S:Eu opaque screen 91 μm thick [9]. The DQE values of 460 and 220 μm LuPO₄:Eu films at low frequencies (0–2 cycles mm⁻¹) are comparable and even higher than the DQE values of the Gd₂O₂S:Eu screen. Yet, for higher frequencies the DQE is clearly higher for the Gd₂O₂S:Eu screen. This might reflect a better uniformity of the LuPO₄:Eu films (Fig. 2) compared to the Gd₂O₂S:Eu powder screen. The latter sedimented much faster due to the large particles, while the former, being nanocrystalline, sedimented very slowly. And this is the uniformity of a screen which affects the low frequencies noise properties mainly [26, 27]. Indeed, according to Tamatani et al. [28], nanosized spherical particles, like in our LuPO₄:Eu, offer much more uniform packing, improved compactness and thus, higher effective

density than in the case of the coarse, micron-sized phosphor. On the other hand, because of the higher MTF of Gd₂O₂S:Eu screen and its good noise properties it outperforms the LuPO₄:Eu thicker films (460 and 220 μm) in the overall image quality for 2–10 cycles mm⁻¹ frequencies. Comparing the Gd₂O₂S:Eu screen with the thinner LuPO₄ films (67 and 100 μm), the DQE of Gd₂O₂S:Eu is higher for the whole range of frequencies because of its better noise properties. One point that can explain the better noise properties of Gd₂O₂S:Eu screen is its higher luminescence efficiency under similar irradiation conditions as shown by Michail et al. [15].

Acknowledgments This research has been supported by the Marie Curie Initial Training Networks (ITN) action under the LUMINET project Grant Agreement No. 316906 and partially by Wrocław Research Centre EIT+ within the project “The Application of Nanotechnology in Advanced Materials”—NanoMat (POIG.01.01.02-02-002/08) co-financed by the European Regional Development Fund (Innovative Economy Operational Program 1.1.2). J.Z. appreciates support from Operational Programme Human Capital No. UDA-POKL.04.01.01-00-054/10-01 09 project “Development of the potential and educational offer of the University of Wrocław—the chance to enhance the competitiveness of the University” co-funded by European Union within the European Social Fund. Activity 4.1. Sub-activity 4.1.1.

Open Access This article is distributed under the terms of the Creative Commons Attribution 4.0 International License (<http://creativecommons.org/licenses/by/4.0/>), which permits unrestricted use, distribution, and reproduction in any medium, provided you give appropriate credit to the original author(s) and the source, provide a link to the Creative Commons license, and indicate if changes were made.

References

1. G.G. Blasse, B.C. Grabmaier, *Luminescent Materials* (Springer, Berlin, 1994)
2. A. Lempicki, C. Brecher, P. Szupryczynski, H. Lingertat, V.V. Nagarkar, S.V. Tipnis, S.R. Miller, Nucl. Instrum. Methods A **488**(3), 579 (2002)
3. V.V. Nagarkar, S.V. Tipnis, S.R. Miller, A. Lempicki, C. Brecher, P. Szupryczynski, H. Lingertat, IEEE Trans. Nucl. Sci. **50**(3), 297 (2003)
4. A. Krell, J. Klimke, T. Hutzler, Opt. Mater. **31**(8), 1144 (2009)
5. R. Apetz, M.P.B. Van Bruggen, J. Am. Ceram. Soc. **86**(3), 480 (2003)
6. B. Kingery, H.K. Bowen, *Introduction to Ceramics* (Wiley, New York, 1976)
7. A. Krell, P. Blank, H. Ma, T. Hutzler, M. Van Bruggen, R.J. Apetz, Am. Ceram. Soc. **86**(1), 12 (2003)
8. P.F. Liaparinos, J. Biomed. Opt. **17**(12), 126013 (2012)
9. I. Seferis, C. Michail, I. Valais, J. Zeler, P. Liaparinos, G. Fountos, N. Kalyvas, S. David, F. Stromatia, E. Zych, I. Kandarakis, G. Panayiotakis, J. Lumin. **151**, 229 (2014)
10. L. Pidol, A. Kahn-Harari, B. Viana, E. Virey, B. Ferrand, P. Dorenbos, J.T.M. de Haas, C.W.E. van Eijk, IEEE Trans. Nucl. Sci. **51**(3), 1084 (2004)

11. M. Balcerzyk, M. Moszynski, Z. Galazka, M. Kapusta, A. Syntfeld, J.L. Lefaucheur, IEEE Nucl. Sci. Symp. Rec. **2**, 986 (2004)
12. C. Mansuy, J.M. Nedelec, C. Dujardin, R. Mahiou, J. Sol-Gel. Sci. Technol. **38**(1), 97 (2006)
13. C.M. Michail, I.G. Valais, A.E. Toutountzis, N.E. Kalyvas, G.P. Fountos, S.L. David, I.S. Kandarakis, G.S. Panayiotakis, IEEE Trans. Nucl. Sci. **55**(6), 3703 (2008)
14. J.M. Boone, Physics and psychophysics, in *Handbook of Medical Imaging*, vol. 1, ed. by J. Beutel, H.L. Kundel, R.L. Van Metter (SPIE Press, Bellingham, 2000), pp. 36–57
15. C.M. Michail, G.P. Fountos, P.F. Liaparinos, N.E. Kalyvas, I. Valais, I.S. Kandarakis, G.S. Panayiotakis, Med. Phys. **37**(7), 3694 (2010)
16. J.H. Hubbel, S.M. Seltzer, Tables of X-ray mass attenuation coefficients and mass energy absorption coefficients 1 keV to 20 MeV for elements $Z = 1$ to 92 and 48 additional substances of dosimetric interest, U.S. Department of Commerce, NISTIR Report No. 5632 (1995)
17. S. David, C. Michail, I. Seferis, I. Valais, G. Fountos, P. Liaparinos, I. Kandarakis, N. Kalyvas, J. Lumin. **169**(Part B), 706 (2016)
18. C. Michail, I. Valais, I. Seferis, N. Kalyvas, G. Fountos, I. Kandarakis, Radiat. Meas. **74**, 39 (2015)
19. N.W. Marshall, Phys. Med. Biol. **51**(10), 2441 (2006)
20. J.T. Dobbins III, Physics and psychophysics, in *Handbook of Medical Imaging*, vol. 1, ed. by J. Beutel, H.L. Kundel, R.L. Van Metter (SPIE Press, Bellingham, 2000), pp. 161–222
21. I.E. Seferis, C.M. Michail, I. Valais, G.P. Fountos, N.I. Kalyvas, F. Stromatia, G. Oikonomou, I.S. Kandarakis, G.S. Panayiotakis, Nucl. Instrum. Methods A **729**, 307 (2013)
22. L. Ayala-Domínguez, M.E. Brandan, Radiat. Meas. **59**, 176 (2013)
23. J.R. Greening, *Fundamentals of Radiation Dosimetry* (IOP, London, 1985)
24. P.F. Liaparinos, I.S. Kandarakis, D.A. Cavouras, H.B. Delis, G.S. Panayiotakis, Med. Phys. **33**(12), 4502 (2006)
25. P.F. Liaparinos, I.S. Kandarakis, D.A. Cavouras, H.B. Delis, G.S. Panayiotakis, Med. Phys. **34**(5), 1724 (2007)
26. H. Arimura, M. Yamada, M. Matsumoto, H. Kanamori, J. Photogr. Sci. **40**(1), 6 (1992)
27. N. Kalivas, L. Costaridou, I. Kandarakis, D. Cavouras, C.D. Nomicos, G. Panayiotakis, Nucl. Instrum. Methods A **490**(3), 614 (2002)
28. M. Tamatani, N. Matsuda, M. Okumura, A. K. Albessard, Y. Inoue, S. Yokota, in *Proceedings of the Sixth International Conference on Luminescent Materials*, vol. 97(29) (The Electrochemical Society, 1998), pp. 11–21